Bioactive Materials 6 (2021) 2647–2657

Contents lists available at ScienceDirect

Bioactive Materials

journal homepage: www.sciencedirect.com/journal/bioactive-materials

Polydopamine nanoparticle-dotted food gum hydrogel with excellent antibacterial activity and rapid shape adaptability for accelerated bacteria-infected wound healing

Qiankun Zeng [a,b,1], Yuna Qian [a,b,1], Yijing Huang [a], Feng Ding [c], Xiaoliang Qi [a,b,**], Jianliang Shen [a,b,*]

[a] State Key Laboratory of Ophthalmology, Optometry and Vision Science, School of Ophthalmology and Optometry, School of Biomedical Engineering, Wenzhou Medical University, Wenzhou, Zhejiang, 325027, China
[b] Engineering Research Center of Clinical Functional Materials and Diagnosis & Treatment Devices of Zhejiang Province, Wenzhou Institute, University of Chinese Academy of Sciences, Wenzhou, Zhejiang, 325000, China
[c] Department of Microbiology & Immunology, School of Basic Medical Sciences, Wenzhou Medical University, Wenzhou, Zhejiang, 325035, China

ARTICLE INFO

Keywords:
Wound healing
Polydopamine nanoparticles
Food gum hydrogel
Shape adaptability
Photothermal treatment

ABSTRACT

Most commonly used wound dressings have severe problems, such as an inability to adapt to wound shape or a lack of antibacterial capacity, affecting their ability to meet the requirements of clinical applications. Here, a nanocomposite hydrogel (XKP) is developed by introducing polydopamine nanoparticles (PDA NPs) into a food gum matrix (XK, consisting of xanthan gum and konjac glucomannan, both FDA-approved food thickening agents) for skin wound healing. In this system, the embedded PDA NPs not only interact with the food gum matrix to form a hydrogel with excellent mechanical strength, but also act as photothermal transduction agents to convert near-infrared laser radiation to heat, thereby triggering bacterial death. Moreover, the XKP hydrogel has high elasticity and tunable water content, enabling it to adapt to the shape of the wound and insulate it, providing a moist environment suitable for healing. *In-vivo* skin wound healing results clearly demonstrate that XKP can significantly accelerate the healing of wounds by reducing the inflammatory response and promoting vascular reconstruction. In summary, this strategy provides a simple and practical method to overcome the drawbacks of traditional wound dressings, and provides further options when choosing suitable wound healing materials for clinical applications.

1. Introduction

Millions of wounds caused by accidental trauma or surgical operations require treatment every year [1,2]. Open wounds are susceptible to external bacterial infections, leading to a risk of severe wound inflammation, inhibiting wound healing, and even leading to the risk of death [2,3]. Generally, the wound healing process comprises hemostasis, inflammation, proliferation, and remodeling [4]. At present, wound dressings are one of the most commonly used methods to promote wound healing, owing their ease of application and significant therapeutic effects. Although gauze [5], adhesive bandages [6], and cotton [7] are widely used as wound dressings in clinical treatments, these materials have some severe problems in practical applications, such as a lack of elasticity [8], which affects their ability to adapt to the shape of the wound and fit tightly, especially when deform as the body parts undergo frequent movements. In addition, most wound dressings lack sufficient antibacterial power or require a large amount of antibiotics, the use of which may increase the resistance of bacteria [9,10]. Therefore, it is of great practical significance to develop an antibacterial wound dressing that quickly adapts to the correct shape and does not use

Peer review under responsibility of KeAi Communications Co., Ltd.
* Corresponding author. State Key Laboratory of Ophthalmology, Optometry and Vision Science, School of Ophthalmology and Optometry, School of Biomedical Engineering, Wenzhou Medical University, Wenzhou, Zhejiang, 325027, China.
** Corresponding author. State Key Laboratory of Ophthalmology, Optometry and Vision Science, School of Ophthalmology and Optometry, School of Biomedical Engineering, Wenzhou Medical University, Wenzhou, Zhejiang, 325027, China.
E-mail addresses: xiaoliangqi90@gmail.com (X. Qi), shenjl@wiucas.ac.cn (J. Shen).
[1] These authors contributed equally to this work.

https://doi.org/10.1016/j.bioactmat.2021.01.035
Received 9 October 2020; Received in revised form 22 January 2021; Accepted 29 January 2021
Available online 12 February 2021

antibiotics.

Hydrogels, which are interconnected polymeric networks with high water content [11–13], are widely recognized as ideal materials for wound dressings [14,15]. A synergistic hydrogel can be produced by mixing xanthan gum (XG) and konjac glucomannan (KGM), which is a typical food gum material [16] that has already been approved by the US FDA [17]. Separately, XG and KGM exist in a solution state. However, when they are mixed, significant non-covalent interactions are generated between the XG and KGM polysaccharide chains, forming a thermoreversible gel network [18]. Compared with most hydrogels, XG–KGM (XK) gels have higher elasticity and water content, enabling rapid shape adaptability in response to external changes. This ensures that the XK gels can perfectly fit the size and shape of the wound, insulating it from the outside world and providing a moist environment for healing. However, although XK hydrogel dressings exhibit satisfactory wound healing properties, they cannot meet the needs of practical applications when used alone. This is because they lack the antibacterial ability required to reduce wound infections, and have insufficient mechanical strength, so are prone to rupture at wound sites [19].

Doping with nanophase polydopamine (PDA NPs) is a potential means to compensate for the defects of XK gels. Mussel-type PDA NPs prepared through the oxidative polymerization of dopamine have excellent properties for applications in the biomedicine [20,21]. The structure of PDA NPs is like that of natural melanin, and its advantages include strong light absorption capacity, good biocompatibility, and a simple preparation method [22,23]. PDA NPs also have a high photothermal conversion efficiency and have recently been developed as a photothermal transduction agent to prevent bacterial infections [24,25]. Nanocomposite XK- PDA (XKP) hydrogels, produced by doping XK gels with PDA NPs, can be used to kill bacteria in wounds through photothermal sterilization and show broad-spectrum bactericidal activity without causing bacterial drug resistance. Moreover, PDA NPs can interact with the XK gel matrix to form a nanocomposite hydrogel with high mechanical strength and prevent the hydrogel network from rupture under mechanical stress [26].

Drawing on these results, we synthesized a series of innovative nanocomposite hydrogels by doping PDA NPs into XK gels in situ to enhance the healing of bacteria-infected wounds. The XKP nanocomposite hydrogels showed rapid shape adaptability, ensuring that the dressing fit the shape of the wound completely. The XKP hydrogel could also produce photothermal effects when exposed to near-infrared (NIR) light, thereby killing bacteria at the wound site, reducing inflammation, and ultimately promoting wound healing [27]. In this hydrogel system, PDA NPs and XK gels work together to achieve the desired functions. On the one hand, PDA NPs enhance the mechanical properties of the gel to prevent rupture and address the problem of the gel's lack of antibacterial effects. On the other hand, XK gels have porous structures, which can provide sufficient space to accommodate PDA NPs. The XKP hydrogel dressings fabricated in this study combine the remarkable antibacterial activity of PDA NPs with the rapid shape adaptability of the XK hydrogel. This strategy provides more options in choosing an appropriate wound dressing and can facilitate the clinical translation uptake of new functional dressings for treating bacterial infection in wounds.

2. Materials and methods

2.1. Materials

Dopamine (DA) was bought from Engery Chemical (Shanghai, China). Xanthan gum (XG) and konjac glucomannan (KGM) were purchased from Aladdin (Shanghai, China). Dulbecco's modified Eagle medium (DMEM), phosphate buffered saline (PBS), fetal bovine serum (FBS), and cell counting kit-8 (CCK-8) were purchased from Gibco (Thermo Fisher Scientific). All reagents and materials were all analytical purity and were used as received without purification.

2.2. Synthesis of PDA NPs

First, 40 mL ethanol was mixed with 90 mL deionized water and 2 mL aqueous ammonia solution (28–30%) under mild magnetic stirring at 30 °C for 0.5 h. Next, 0.5 g DA powder was dissolved in 10 mL deionized water and added to the mixed solution with stirring for another 24 h. Finally, the PDA NPs were collected by centrifugation (12000 rpm, 8 min) and washed three times with deionized water.

2.3. Preparation of XKP nanocomposite hydrogel

Briefly, 1.0% XG and 1.0% KGM solutions (w/v) were prepared. Then, a mixed solution with XG:KGM ratio of 4:6 was heated at 80 °C for 30 min to ensure uniform mixing. Subsequently, PDA NPs were dispersed in samples of the XK solution to obtain final concentrations of 0, 0.5, 1, and 2 mg/mL. The resulting mixtures were denoted XK, XKP0.5, XKP, and XKP2, respectively. Finally, the mixtures were transferred to clean petri dishes and cooled to room temperature to form gel networks.

2.4. Characterization of samples

The morphology of PDA NPs was measured using a JEM-1230 transmission electron microscope (TEM) with an accelerating voltage of 100 kV, and the hydrodynamic size was determined by dynamic light scattering. Three-dimensional structures of the XKP composite hydrogel were studied using a scanning electron microscope (SEM, SU8010, Hitachi, Japan) at an acceleration voltage of 5 kV. Fourier transform infrared (FTIR) spectra of XG, KGM, PDA NPs, XK, and XKP were recorded in the range 4000–400 cm^{-1} using a Thermo Fisher Nicolet IS-10 spectrometer. Thermogravimetric analysis (TGA) of XG, KGM, PDA NPs, XK, and XKP was conducted using a thermal analyzer (PerkinElmer, TGA 8000).

2.5. Swelling behavior of hydrogels

The gravimetric method was used to investigate the swelling performance of hydrogels in PBS at 37 °C. Briefly, freeze-dried hydrogel samples with known weight (Wd) were first swollen in PBS. At predetermined time points, the hydrated hydrogels were removed from the PBS, and the hydrated hydrogel weight (W_t) was recorded after removing excess liquid from the gel surface with wet filter paper. This procedure was repeated until a swelling equilibrium was obtained. The swelling ratio (SR) was defined as follows:

$$SR = W_t/W_d$$

2.6. Measurements of photothermal performance

The photothermal effects of PBS, XK, XKP0.5, XKP, and XKP2 were measured using the following steps. All samples (1.0 mL) were prepared in 1.5 mL centrifuge tubes and irradiated with an 808 nm laser (1 W/cm^2, 10 min). Thermal images were captured using an infrared thermometer (E4, FLIR, USA). Subsequently, the effects of laser intensity (0.5, 1.0, and 2.0 W/cm^2) on the photothermal efficiency of the XKP group were investigated. Finally, the photothermal stability of XKP was explored using an on–off laser cycle four times.

2.7. In-vitro antibacterial tests

The *in-vitro* antibacterial ability of XKP was evaluated using the spread plate method. First, 80 μL of hydrogel precursor solution (XK or XKP) was transferred to a 96-well plate, and gelation was carried out at 25 °C for 1 h. Samples of *Escherichia coli* (*E. coli*, ATCC 25922) and

Staphylococcus aureus (*S. aureus*, ATCC 29213) were prepared at concentrations of about 1.0×10^6 CFU/mL. Then 200 μL of the bacterium solution was added to the as-prepared XKP hydrogel, and exposed to an 808 nm laser (1 W/cm^2) for 10 min. Finally, the numbers of remaining bacteria were determined using the spread plate method, and the viable colony units on the plates were photographed.

2.8. Mechanical performance tests

The mechanical performances of XK and XKP were tested using a commercial rheometer (TA Instruments, DHR-2) and an electronic universal testing machine. For rheological evaluation, linear viscoelastic regions of gels were obtained from dynamic strain sweeps. Dynamic frequency sweep measurements were determined under a fixed strain of 1% over a range of 0.1–10 Hz. Compression strain tests of gel samples (height, 20 mm; diameter, 25 mm) were performed at a compression rate of 2 mm/min.

2.9. Hemolytic tests

In brief, 500 μL of rat blood was centrifuged at 3500 rpm for 5 min and then washed with PBS three times (giving a final concentration of 5%). Subsequently, 250 mg hydrogel samples (XK or XKP) were mixed with 500 μL erythrocytes in a tube. After incubation for 60 min at 37 °C with a shaking speed of 100 rpm, all samples were centrifuged at 3500 rpm for 5 min. The absorbance of the liquid supernatant at 545 nm was determined using a microplate reader (Thermo Fisher Scientific Oy, Vantaa, Finland). PBS was used as a negative control, and deionized water was used as a positive control. The hemolysis percentage of samples was calculated by the following equation:

$$\text{Hemolysis ratio } (\%) = [(OD_s - OD_p)/(OD_w - OD_p)] \times 100\%$$

where OD_s, OD_p, and OD_w represent the absorbances of the sample, PBS, and deionized water, respectively.

2.10. Cytocompatibility evaluation of the samples

The cytotoxicities of XK and XKP were evaluated using a direct contact test between gel samples and L929 cells (mouse fibroblasts). A sterile gel dish with a diameter of 5 mm and a thickness of about 1.5 mm was prepared. The complete growth medium was prepared with DMEM, 10% PBS, 100 mg/L streptomycin, and 1.0×10^5 U/L penicillin. To evaluate the cytotoxicity of samples, hydrogel disks were cultured with L929 cells in a 96-well plate. At predetermined time periods, a CCK-8 assay was performed on the cells, and the absorbance was measured at a wavelength of 450 nm. The cell viability was calculated as:

$$\text{Cell viability } (\%) = A450_{sample}/A450_{control} \times 100\%$$

A live/dead viability assay was carried out to further evaluate the cytotoxicity of samples. The L929 cells were seeded in a 20 mm glass-bottomed cell culture dish and co-cultured with samples. After 3 days, cells were stained with propidium iodide (red) and calcein-AM (green), and observed under a confocal microscope (Nikon, Japan).

2.11. Hemostasis performance of the hydrogels

A rat-tail amputation model was employed to evaluate the hemostatic performance of the hydrogels. First, a 250 g rat was anesthetized, and a 2 cm cut was made in its tail with surgical scissors. The rat was placed in air for 15 s to ensure normal bleeding. Then, gauze, XK, and XKP were immediately applied with pressure to the bleeding areas, and the blood was absorbed using a filter paper. After 10 min, the weight of samples and filter papers were measured. In the control group, no treatment was applied after cutting the tail. All tests were repeated three times for each group.

2.12. In-vivo wound healing experiments

All animal experiments were approved by the Animal Ethics Committee of Wenzhou Medical University (approved number Wydw7019-0134). Male Sprague-Dawley (Beijing Vital River Laboratory Animal Technology Co., Ltd) rats (6 weeks old) with an average weight of almost 250 g were used for *in-vivo* studies. First, after a standard anesthesia procedure, the fur was shaved from the backs of rats. A full-thickness round skin wound with a diameter of 8 mm was created using a hole punch. Next, 20 μL of *E. coli* solution (5×10^7 CFU/mL) was added to the surface of the wound, and the bacteria-infected wound model was formed after 24 h of infection. PBS, XK, and XKP were separately transferred onto the wounds, and an 808 nm laser (1 W/cm^2) was used to irradiate the wound site for 10 min. The temperature change of the wound site was recorded using an infrared thermometer (E4, FLIR, USA). On days 0, 3, 7, and 14, the wound area was photographed and the corresponding wound contraction was calculated.

2.13. Histological analysis

To evaluate wound closure performance of XKP hydrogel, wound tissue samples were collected and fixed with 4% paraformaldehyde for 1 h. After embedding in paraffin, the samples were cut into slices of 4 μm thickness. Subsequently, all slices were stained with either hematoxylin and eosin (H&E, Beyotime) or Masson trichrome stain (Beyotime). Finally, all slices were observed and photo graphed under an optical microscope. In addition, the fixed and frozen sections were stained with CD31 and TNF-α, and the nuclei were stained with 4′,6-diamidino-2-phenylindole (DAPI). Staining was observed under a fluorescence microscope (Olympus CKX53, Tokyo, Japan).

2.14. Statistical analysis

All quantitative results are shown as the mean ± standard deviation (SD) from at least three independent experiments. Statistical analysis was performed using Student's t-test. Differences were considered statistically significant at $p < 0.01$ (**), $p < 0.001$ (***) and $p > 0.05$ (No significant, NS).

3. Results and discussion

3.1. Preparation and characterization of XKP nanocomposite hydrogels

Scheme 1 exhibits the fabrication process for the XKP nanocomposite hydrogels and their application in wound healing. In brief, PDA NPs were uniformly mixed into a homogeneous mixture of XG and KGM in deionized water. The mixture was then transferred into a clean Petri dish and cooled to room temperature to form XKP nanocomposite hydrogels (Scheme 1A). In this system, PDA NPs were obtained through self-polymerization of dopamine under alkaline conditions [28], and the hydrogel was formed based on the synergistic gelation mechanism of XG and KGM [29]. We expected that the resulting XKP nanocomposite hydrogels would have excellent antibacterial activity, biocompatibility, and shape adaptability that would enhance bacteria-infected wound healing (Scheme 1B).

TEM and SEM images of PDA NPs show that they have a relatively uniform size with nanoscale dimensions (Fig. 1A and Fig. S1A) and that their surfaces are rough (Fig. 1B and Fig. S1B). Dynamic light scattering indicates a narrow size distribution of PDA NPs in deionized water, with an average hydrodynamic diameter of 179 nm (Fig. 1C). SEM was used to observe the microstructures of XK and XKP. As shown in Fig. 1D and E, both XK and XKP show a bamboo-like hierarchical structure with well-ordered macropores. Each node consists of an internal diaphragm and an external ridge that could absorb and disperse most of the energy from external forces [30], preventing the hydrogel from breaking. This enables highly elastic behaviors that are beneficial to dressing materials.

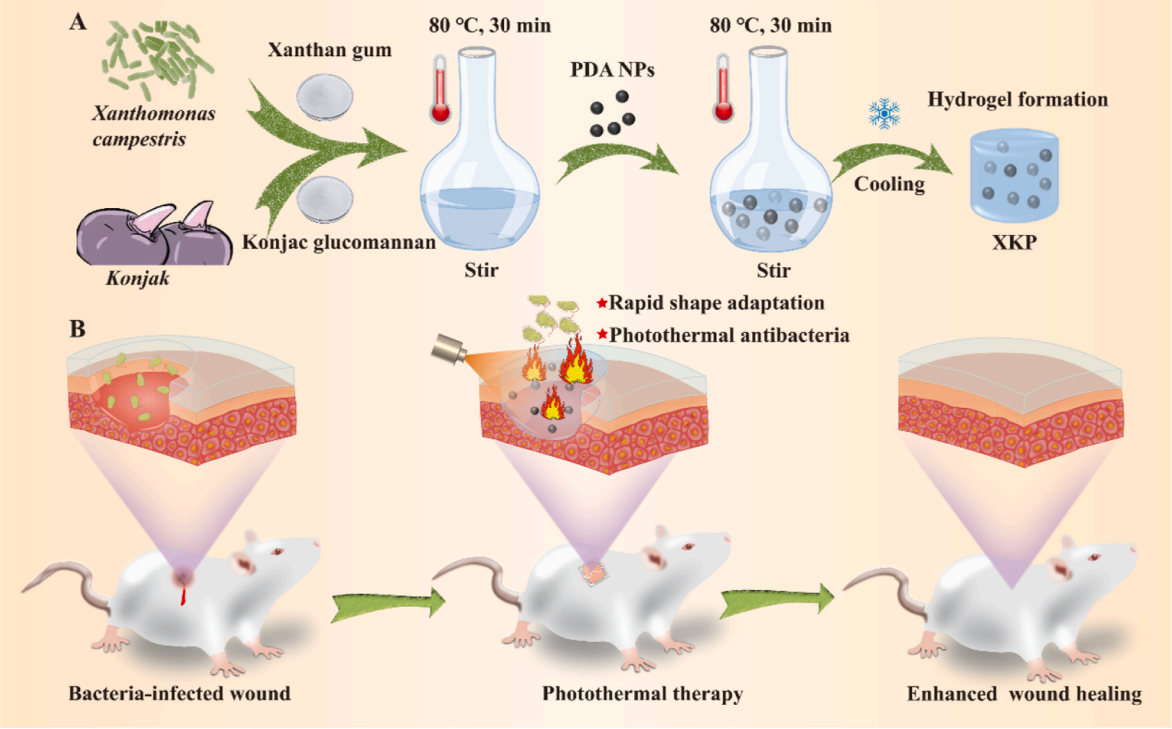

Scheme 1. (A) Preparation and (B) application of XKP nanocomposite hydrogels in bacteria-infected wound healing.

Moreover, high-magnification SEM (Fig. 1F) shows that PDA NPs are dotted in the interior of XKP matrix, while XK, without PDA NPs, has a smooth surface (Fig. S2). As previously reported [31], the mechanical properties of a hydrogel can be significantly improved by interactions between PDA NPs and the hydrogel matrix. Therefore, we expected that doping with PDA NPs would further enhance the mechanical properties of the resulting hydrogel. Elemental mapping analysis (Fig. 1G–I) demonstrates the uniform distribution of PDA NPs within the gel (as these contain nitrogen), while oxygen and carbon are found in both gels and PDA NPs. Finally, the average diameter of the hydrogel pores tends to increase after incorporation of PDA NPs (Figs. S3A and B), which would help to absorb more wound exudates from wound sites, and may thereby prevent bacterial infection [32].

The chemical structures of the resulting hydrogels were characterized by Fourier transform infrared (FTIR) spectroscopy (Fig. 1J). Characteristic peaks (XK, XKP) at 3336, 2908 and 1022 cm^{-1} could be attributed to O–H, C–H, and C–OH stretching, respectively. PDA NPs showed a peak at 1510 cm^{-1}, which was ascribed to the bending vibrations of indolequinone groups. Absorption bands of all raw materials (XG, KGM, PDA NPs) could be observed in XKP, confirming the successful formation of nanocomposite hydrogels. The thermal properties of XG, KGM, PDA NPs, XK, and XKP were investigated by TGA (Fig. 1K). The TGA curves of XK and XKP show similar trends. After a hydrogel was formed, a decrease in the evaporation temperature of water from 112 °C (XG) to 80 °C (XKP) was probably due to the gel porous networks that facilitated the evaporation of water. The mass loss occurring at 250–350 °C was attributed to the decomposition of the gel network [33]. Figure 1L shows the swelling features of XK and XKP. All the prepared gels absorbed water gradually and achieved equilibrium by the end of the measurement (200 min). Moreover, after the introduction of PDA NPs, the gels showed good water absorption ability, which would facilitate the absorption of wound exudates.

3.2. NIR-photothermal performance

The NIR photothermal performance of the XKP nanocomposite hydrogels was systematically assessed before the *in-vivo* antimicrobial and repair experiments. As shown in Fig. 2A, the XKP hydrogel demonstrates strong NIR light absorption, indicating that it possesses excellent NIR photothermal properties. Therefore, we evaluated the photothermal conversion efficiency of the XKP hydrogel using a NIR laser (808 nm), with phosphate-buffered saline (PBS) as a control. Temperature–NIR irradiation time curves and heat maps for the XKP nanocomposite hydrogel are shown in Fig. 2B and C, respectively. After 10 min of NIR irradiation, there was no noticeable temperature increase for the XK hydrogel, whereas the temperatures of the XKP0.5, XKP, and XKP2 hydrogels (with PDA NPs contents of 0.5, 1, and 2 mg/L, respectively) increased instantly. Furthermore, the rate at which the temperatures of the XKP hydrogels increased depended on the amount of PDA NPs used for doping. More specifically, for PDA NPs contents of 0, 0.5, 1, and 1.5 mg/mL, the temperatures achieved were 28.3, 48.1, 59.9, and 78.9 °C, respectively, indicating that XKP nanocomposite hydrogels have excellent photothermal properties. According to data published by other researchers [4,34], bacteria are killed by the denaturing of proteins and enzymes when exposed to temperatures above 50 °C. Considering the optimum antibacterial temperature, we selected XKP as a representative example for all subsequent experiments. When the power density varied from 0.5 to 2.0 W/cm^2, the temperature of XKP gradually increased from 45.1 to 75.6 °C (Fig. 2D), demonstrating the adjustability of its photothermal performance. Moreover, we found that XKP possessed excellent photostability, with hardly any reduction in the final temperature after four laser on–off cycles (Fig. 2E). These results confirm that XKP has strong photothermal performance and demonstrate its suitability for antimicrobial applications with photothermal therapy.

3.3. In-vitro NIR photothermal antimicrobial activity

The excellent photothermal performance of the XKP nanocomposite hydrogel inspired us to investigate its antibacterial activity. The NIR-induced photothermal antibacterial abilities of XKP and XK were evaluated against *E. coli* and *S. aureus*. As indicated by the representative

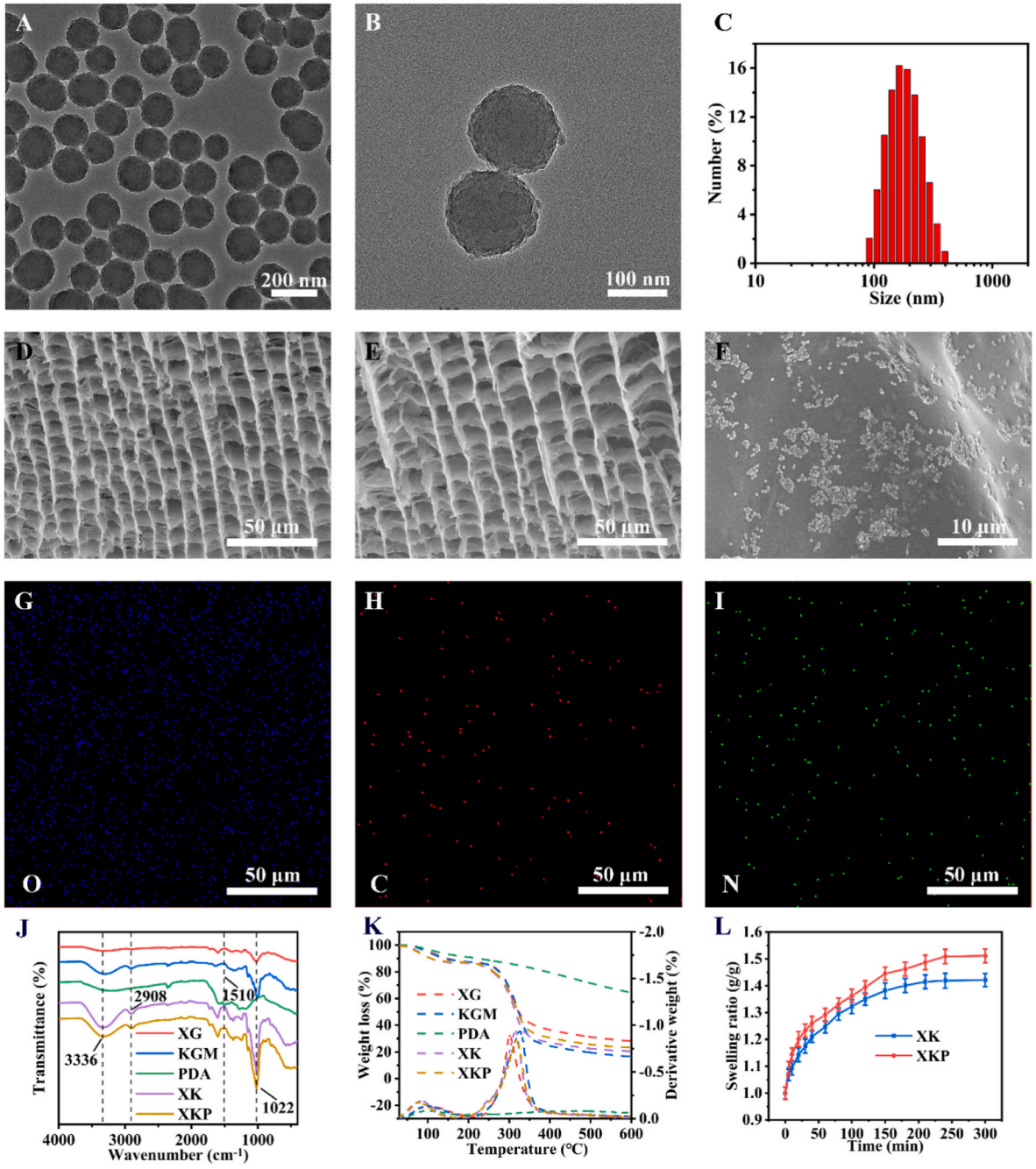

Fig. 1. Physical and chemical properties of PDA NPs, XK, and XKP. (**A**, **B**) TEM images and (**C**) size distribution of PDA NPs. SEM images of XK (**D**) and XKP (**E**). (**F**) High-magnification micrograph of XKP. (**G–I**) Elemental mapping analysis of XKP (SEM). (**J**) FTIR spectrum and (**K**) TGA curve of XG, KGM, PDA NPs, XK and XKP. (**L**) Swelling ratio of wet XK and XKP hydrogels (n = 3).

images shown in Fig. 2F–H, L, and Figure S4A–C, XK did not exhibit antibacterial activity after 10 min of NIR irradiation. While XKP showed excellent antibacterial activity, with killing ratios reaching 98.12% for *E. coli* and 96.64% for *S. aureus*. These results show good agreement with the photothermal conversion data (Fig. 2B), demonstrating the effectiveness of the photothermal antibacterial effect. To further verify the photothermal antibacterial effect of XKP, fluorescence staining of bacteria was performed after the NIR irradiation. Specifically, live bacteria were labeled with SYTO 9 (a nucleic acid stain) to produce green fluorescence, and dead bacteria were labeled with propidium iodide (which shows red fluorescence, owing to the destruction of the cell membrane). As expected, the results are similar to the spread plate images. As shown in Fig. 2I–K and Figs. S4D–F, the PBS and XK groups show almost all green fluorescence after 10 min of NIR irradiation. By contrast, in the XKP group, most of the green fluorescence disappears and a strong red fluorescence appears, suggesting that photothermal therapy could effectively rupture cytoplasmic membranes and induce the death of bacteria. In addition, SEM was used to investigate the morphology of *E. coli* and *S. aureus*. As shown in Fig. 2M – O and Figs. S4G–I, after treatment with NIR, bacteria incubated with PBS and XK had smooth and intact membranes, while bacteria cultured with XKP showed many wrinkles and disruptions. All these results confirm that the NIR-induced photothermal activation of XKP nanocomposite hydrogel induces cell membrane damage, demonstrating the potential to prevent bacterial infections during wound healing.

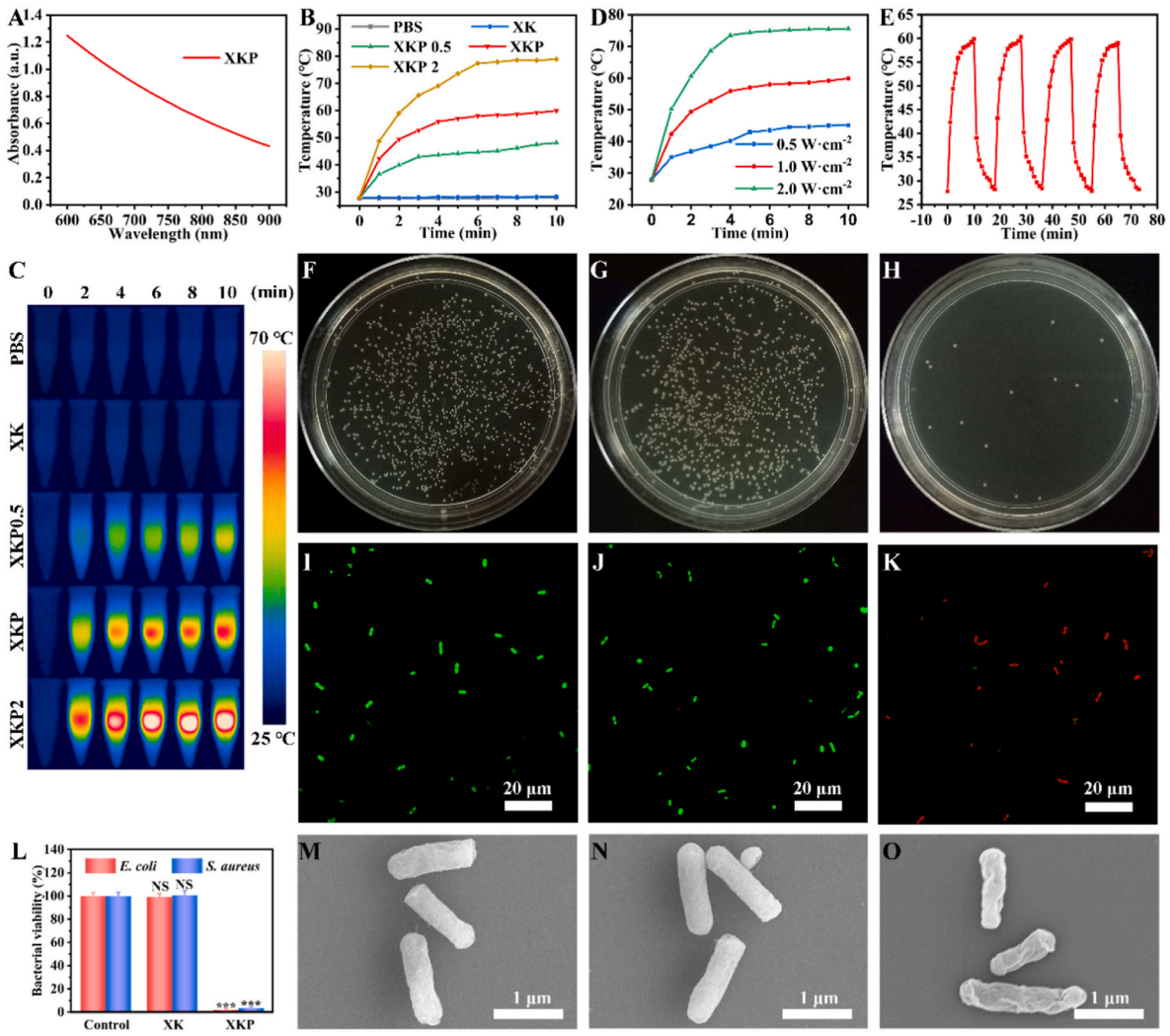

Fig. 2. Near-infrared photothermal and antimicrobial performance of control, XK, and XKP *in vitro*. (**A**) Absorbance spectrum of XKP in the visible and NIR. (**B**) Photothermal effect curves and (**C**) heat maps of XK hydrogels (with PDA NPs contents of 0.5, 1, and 2 mg/L, respectively). (**D**) Temperature changes of XKP for varying power densities of 808 nm laser. (**E**) Irradiation cycle of XKP with 808 nm laser (1 W/cm^2). (**F–H**) Representative images of *E. coli* colony-forming units for (**F**) control, (**G**) XK, and (**H**) XKP, and (**L**) corresponding statistical data of bacterial viability ($n = 3$). (**I–K**) Stained images of live (green fluorescence) and dead (red fluorescence) *E. coli* in (**I**) control, (**J**) XK and (**K**) XKP. (**M–O**) Scanning electron micrographs of *E. coli* in (**M**) control, (**N**) XK, and (**O**) XKP.

3.4. Mechanical properties and deformability

Wounds are frequently deformed by movement or external forces. Hence, strength and elasticity are essential for the application of hydrogels in wound dressings [35]. A macroscopic compression experiment showed that the XKP gel model could withstand tremendous pressure (900 g) without breaking and quickly return to its initial state within 1 s (Fig. S5). This rapid shape adaptability of XKP can be ascribed to two factors. On the one hand, XKP has low substance content (including 0.4% XG, 0.6% KGM, and 0.1% PDA NPs), high porosity, and a strong swelling property (as verified in the characterization of the XKP hydrogel). In this case, the free and reversible movement of water in gel channels is the potential driving force of fast structure recovery [36]. On the other hand, PDA NPs contain a large number of functional groups on their surfaces that could interact with polysaccharide chains, serving as cross-linking sites to increase the mechanical strength of the XK hydrogel, preventing it from breaking under pressure [26]. The compression–recovery process is illustrated in Fig. 3. As shown in Fig. 3A, XKP contains plenty of dynamic water and the corresponding gel channels and inner gel walls are reinforced by PDA NPs. Under pressure, compressive forces cause structural deformation of the gel wall, and thus dynamic water moves to areas where the pressure is reduced, through gel channels (Fig. 3B). When the applied pressure is removed, the dynamic water can move back to its initial position, owing to the swelling driving force of the gel wall, leading to the quick recovery of the entire structure (Fig. 3C). Overall, both the gel network structure and dynamic water have critical roles in the whole compression–recovery process, leading to rapid shape adaptability of XKP. We also conducted rheological experiments to investigate the viscoelasticity features of the prepared hydrogels. As shown in Fig. 3D and E, the values of the storage modulus G′ are larger than those of the loss modulus G″ across the whole range of frequencies tested (0.1–10 Hz), confirming the formation of a stable hydrogel. Moreover, the mechanical properties of the hydrogel improved rapidly after doping with PDA NPs. This occurs because nanophase polydopamine can interact with the hydrogel matrix, increasing the gel stiffness. Similar results were obtained in compression tests (Fig. 3F).

3.5. In-vitro biocompatibility

Favorable biocompatibility is an essential requirement for designing new biomedical materials [37]. As a wound dressing material, the XKP hydrogel will inevitably contact blood. Hence, the blood compatibility of XKP was evaluated using hemolysis experiments. As shown in Fig. 4A,

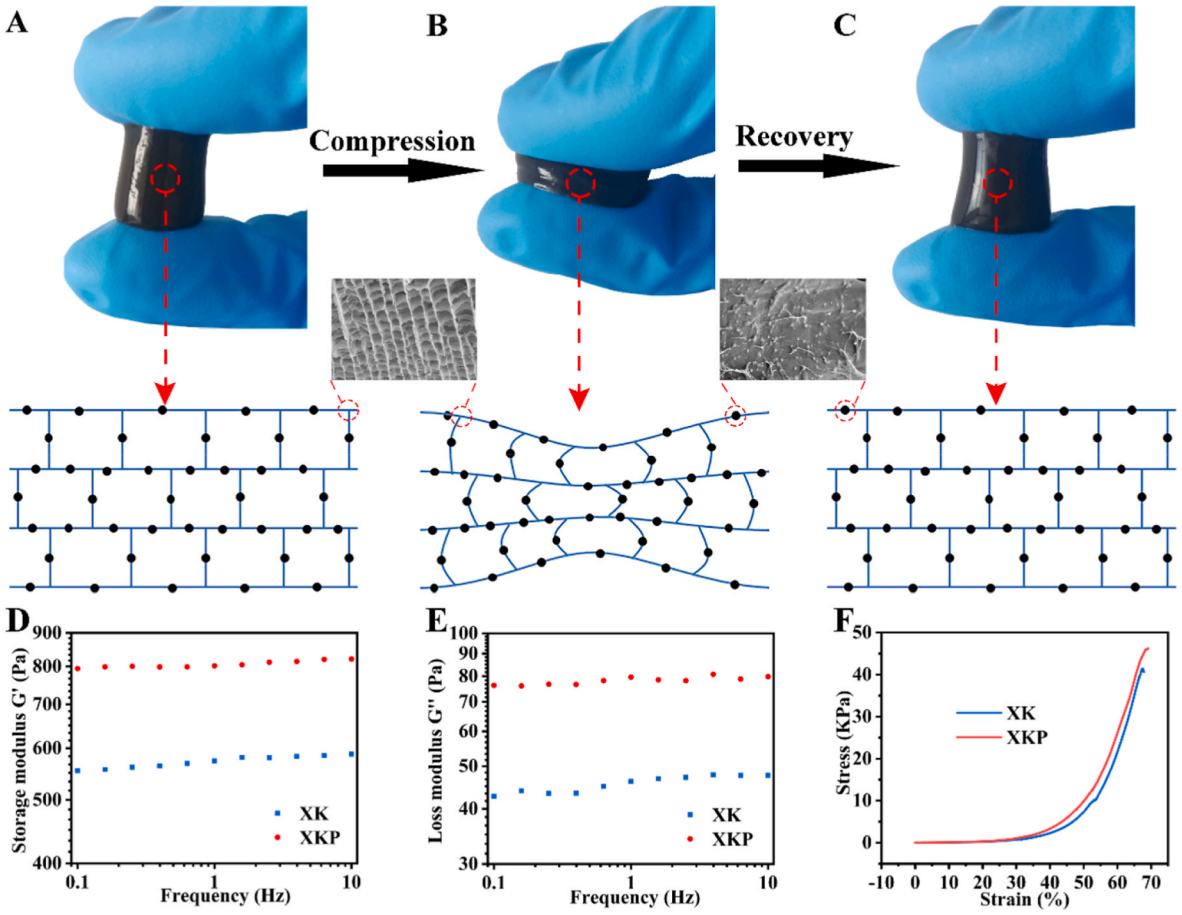

Fig. 3. Deformability and mechanical properties of XK and XKP. Macroscopic phenomenon and microscopic mechanism of XKP (**A**) before compression, (**B**) during compression, and (**C**) on recovery. (**D**) Storage modulus G', (**E**) loss modulus G'', and (**F**) compression tests of XK and XKP.

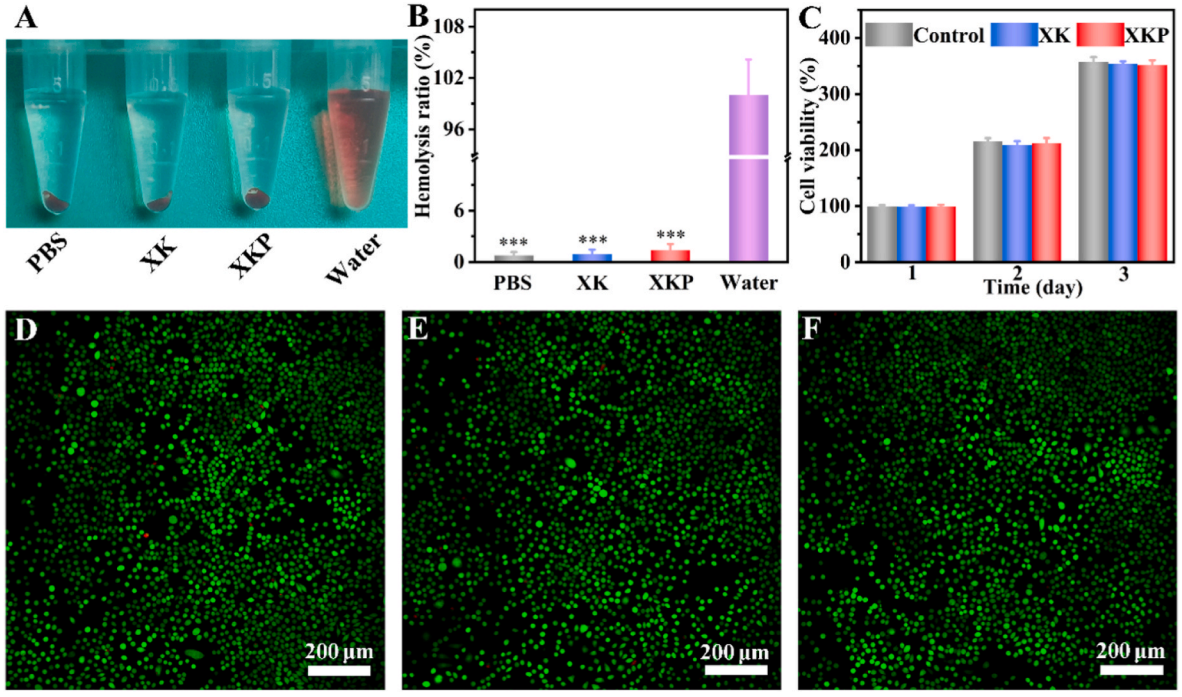

Fig. 4. Biocompatibility evaluation of XK and XKP. (**A**) Hemolysis photographs and (**B**) hemolysis ratio (%) of the hydrogels (n = 3). (**C**) Cell viability of indicated groups co-incubated with L929 cells for 1, 2, and 3 days (n = 3). Live/dead staining of L929 cells after contact with (**D**) control, (**E**) XK and (**F**) XKP for 3 days, where green fluorescence indicates live cells and red fluorescence indicates dead cells.

the positive control group (water) is bright red, whereas XK and XKP appear colorless, similar to the negative control group (PBS). The hemolysis ratios are 0.91% and 1.38% for XK and XKP (Fig. 4B), respectively, indicating the outstanding blood compatibility of the XKP hydrogel. Subsequently, a direct contact assay between the XKP hydrogel and mouse-derived fibroblasts (L929) was employed to investigate the cell compatibility of the XKP hydrogel. After co-incubation for 1, 2, and 3 days, there was no discernible difference in cell viability in the XK and XKP groups com pared with the control group, indicating that the formulated hydrogels had no cytotoxic effects (Fig. 4C). Moreover, the cell compatibility of the XKP hydrogel was further evaluated by a live/dead staining assay. As shown in Fig. 4D–F, most of the cells in the control, XK, and XKP groups were alive (green fluorescence), with only a few dead cells (red fluorescence), confirming the excellent biocompatibility of the XKP hydrogel. Overall, XKP hydrogel possesses excellent blood compatibility and cytocompatibility, indicating that it is a promising candidate for wound healing applications.

3.6. In-vivo NIR photothermal therapy

The previous experiments showed that XKP possesses excellent physicochemical properties, NIR photothermal antimicrobial activity, biocompatibility, and rapid shape adaptability, which help to improve bacteria-infected wound healing. To further evaluate its suitability for application in skin tissue repair, an infectious rat full-thickness defect model was established to confirm the advantages of XKP as a wound dressing *in-vivo*, using PBS and XK as controls (Fig. 5A). Thermal images and temperatures of rats are shown in Fig. 5B and C. The infected wound-site temperature in the control group showed no significant change over 10 min of laser irradiation. By contrast, the temperature in the XKP group rapidly increased from 38.5 °C to 56.1 °C, consistent with the *in-vitro* results. After NIR radiation, bacteria from wound tissue were cultured overnight on LB agar plates. As shown in Fig. S6, there was almost no bacterial growth in XKP group, whereas the control and XK groups still displayed high bacterial growth. These results prove that XKP hydrogel dressing could be used effectively to treat bacterial infection *in vivo*.

3.7. In-vivo wound healing

To further verify the shape adaptability performance of XKP *in-vivo*, we placed the prepared sample in the wound and repeated stretching–extrusion of skin 10 times to simulate the possible deformation of a human wound. As shown in Fig. 5D and S7, XKP varied with the shape of the wound when it was stretched or pressed, and quickly recovered its original shape when the external force on the wound was removed. Furthermore, as can be seen from Fig. S8, the formed XKP hydrogel displayed strong shape adaptability to the surface of porcine skin, as evidenced by its ability to withstand excessive twisting, bending and stretching of the skin. As wounds may be accompanied by excessive loss of blood, an excellent skin wound repair material should possess the ability to stop bleeding. In this work, the hemostatic capacity of the XKP was investigated using a rat-tail amputation model. As shown in Fig. 5F, copious blood flow can be observed in the control rat and the tail dressed with gauze, but this was markedly reduced when XK or XKP was used. The blood loss in the PBS, gauze, XK, and XKP groups (Fig. 5E) were 207.3, 155.7, 38.3 and 16.3 mg, respectively. The excellent hemostatic ability of XKP is mainly attributed to two factors. First, the rapid shape adaptability of XKP enabled it to match the regular or irregular shape of the wound, while XKP served as a container to absorb wound exudates. Second, PDA NPs containing abundant amine and phenolic hydroxyls groups assisted in activating the coagulation system, which induced platelet adhesion and significantly accelerated coagulation [38].

As the most intuitive evaluation indicators, wound area and infection were used to evaluate the repair effects in different groups. Fig. 5G shows representative photographs taken on different days during the wound healing process, exhibiting significant differences between the PBS, XK, and XKP groups. These photographs reveal that a suppurative phenomenon occurred in the PBS and XK groups, resulting in severe inflammation [39]. By contrast, no inflammatory response was observed after XKP treatment, preliminarily indicating the suitability of XKP to treat bacteria-infected wounds. Moreover, a schematic diagram and corresponding quantitative analysis of the wound area over time are shown in Fig. 5H and I. Compared with the PBS group, the XK group showed a significantly enhanced wound repair rate over the whole healing process, indicating that the hydrogel is intrinsically beneficial to wound healing, owing to its rapid shape adaptability. These results suggest that the XKP hydrogel could seal the wound and act as a shield to accelerate wound closure. In particular, the XKP group had a faster rate of wound closure compared with the PBS and XK groups, and even showed fur coverage in the wound site, suggesting that XKP can significantly promote the healing of a bacteria-infected wound.

3.8. Histopathological analysis

To further evaluate wound closure performance of XKP hydrogel, histological analysis of wound sections was performed. The hematoxylin and eosin (H&E) staining results are shown in Fig. 6A and B. The three groups showed varying degrees of healing after treatment for 14 days, with the XKP group showing the best repair effect. The gap in the dermis was largest in the PBS group (4.17 mm), followed by the XK (3.68 mm) and XKP (1.23 mm) groups. Compared with the PBS and XK groups, the XKP group exhibited greater regularity of both epithelium and connective tissue, and new hair follicles could be observed in the wound sites. Magnified images showed that the microscopic skin morphology of the XKP group was closer to that of normal skin, further demonstrating its potent wound healing performance. During wound repair, collagen is the raw material of new tissue; thus, the amount of collagen present can be used as an index to evaluate the repair effect. In Fig. 6C and D, the blue color gradually deepens from the PBS to the XKP group, suggesting that the amount of collagen progressively increased. Moreover, collagen fibers in the PBS group were loosely packed, whereas those in the XK group were densely arranged. By contrast, collagen fibers in the XKP group were dense and ordered, filling the inner area of the granulation tissue with proliferated and migrated fibroblasts. These significant differences between the XKP, PBS, and XK groups demonstrate that collagen deposition is markedly improved by introducing PDA NPs into the XK hydrogel.

Cytokines have been reported to be positively correlated with wound healing, and can indirectly reflect the quality of wound healing [40]. Here, platelet endothelial cell adhesion molecule-1 (CD31) was selected as an indicator to evaluate vascular reconstruction during the regeneration period. As shown in Fig. 6E and S9A, all the therapeutic groups show vascular angiogenesis, but the XKP group is significantly superior to the others in this regard. In addition, immunofluorescence staining of tumor necrosis factor-α (TNF-α) was carried out to verify the inflammation of new tissue. As shown in Fig. 6F and S9B, high TNF-α expression was observed in both the PBS and XK groups, indicating a poor wound-healing effect [35]. However, the expression of TNF-α in the XKP group was lower; this can be attributed to the efficient photothermal antimicrobial activity of XKP, which reduced the inflammatory response. Overall, the immunofluorescence analysis shows that the XKP hydrogel significantly accelerates wound closure by downregulating the expression of TNF-α and upregulating that of CD31.

In summary, in terms of wound closure rate, epithelium integrity, hair follicle growth, collagen deposition, inflammation, and vascular reconstruction, the XKP hydrogel group exhibited better wound healing performance than the PBS group. *In-vivo* histopathological analysis revealed that both the XK hydrogel and the introduction of PDA NPs were beneficial to wound healing. Specifically, the rapid shape adaptation of the XK gels enabled them to fully fit the wound surface, stop

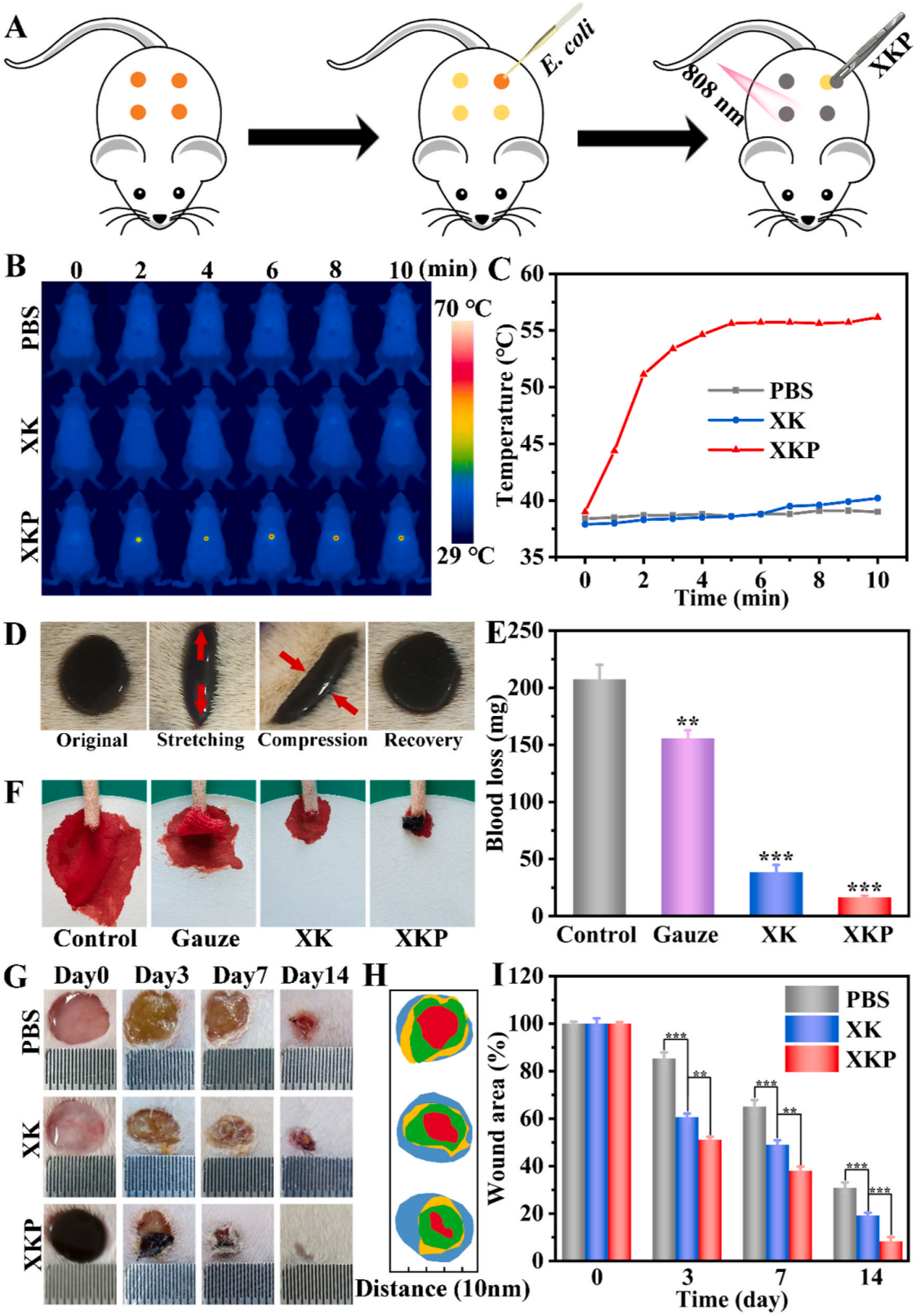

Fig. 5. *In-vivo* assessment of XK and XKP for wound healing. (**A**) Process of creating an infectious rat full-thickness defect model and XKP-induced local photothermal therapy. (**B**) Real-time infrared thermal images and (**C**) photothermal heating curves of XK and XKP with 808 nm laser (1 W/cm^2). (**D**) Shape adaptability performance test of XKP (repeated stretching–compression cycles of skin 10 times; red arrows indicate movement direction of skin). (**E**) Blood loss (n = 3) and (**F**) photographs of amputated rat tails: control, gauze, XK, and XKP. (**G**) Representative skin wound photographs. (**H**) Schematic diagram and (**I**) plot of wound areas (n = 3) for PBS, XK, and XKP groups on days 0, 3, 7, and 14.

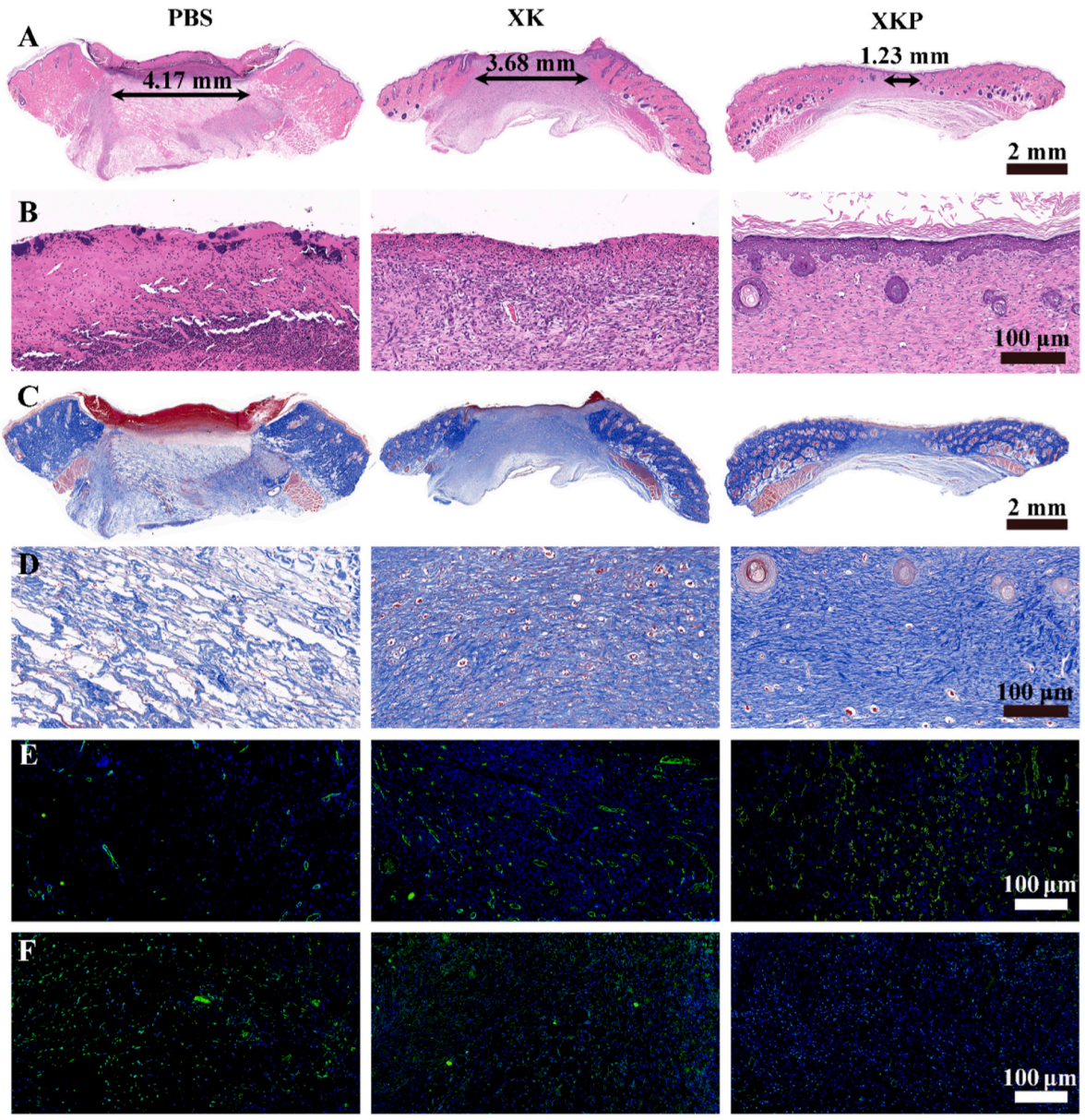

Fig. 6. *In-vivo* histopathological analysis, from left to right: PBS, XK, and XKP. (**A**) H&E staining and (**B**) magnification images. (**C**) Masson's trichrome staining and (**D**) magnification images. Representative photographs of tissue slices after immunofluorescence labeling with (**E**) CD31 and (**F**) TNF-α.

bleeding, and insulate the wound, providing a moist environment for healing to take place, whereas PDA NPs could be used to kill bacteria through photothermal therapy, thereby reducing inflammation at the wound site. Overall, these results demonstrate the great potential of XKP wound dressings.

4. Conclusions

In this work, we successfully designed and developed a PDA NPs-dotted XKP hydrogel with antibacterial properties and rapid shape adaptability for bacteria-infected wound healing. Doping an XK matrix with PDA NPs effectively enhanced the mechanical properties of the obtained hydrogels, and the synthesized XKP hydrogels possessed remarkable and rapid shape adaptability, allowing them to vary with the shape of the wound. *In-vitro* NIR photothermal antibacterial experiments indicated that the XKP hydrogel had broad-spectrum antibacterial activity against both Gram-negative (*E. coli*) and Gram-positive (*S. aureus*) bacteria. Moreover, blood compatibility, live/dead cell staining, and CCK-8 assays showed that XKP possesses excellent blood compatibility and cytocompatibility. In addition to this, XKP could fit well into wounds with a regular or irregular shape, and has an adequate hemostatic ability for treatment of skin trauma. Importantly, the XKP group in our experiments showed a faster rate of wound closure than did the PBS and XK groups, and even grew fur at the wound site, suggesting that XKP can significantly improve the healing of bacteria-infected wounds by reducing inflammation and promoting epidermal regeneration. This XKP hydrogel dressing, prepared using a simple yet practical method, is expected to overcome the problems associated with traditional wound dressings, and has great potential for clinical applications.

CRediT authorship contribution statement

Qiankun Zeng: Conceptualization, Data curation, Formal analysis, Visualization, Writing - original draft. **Yuna Qian:** Conceptualization, Data curation. **Yijing Huang:** Investigation. **Feng Ding:** Methodology. **Xiaoliang Qi:** Project administration, Writing - review & editing. **Jianliang Shen:** Funding acquisition, Project administration.

Declaration of competing interest

The authors declare that they have no known competing financial interests or personal relationships that could have appeared to influence the work reported in this paper.

Acknowledgments

This work was supported by National Natural Science Foundation of China (31800833 and 21977081), Zhejiang Provincial Natural Science of Foundation of China (LZ19H180001 and LQ19C100001), University of Chinese Academy of Sciences (WIBEZD2017001-03 and WIUCASYJ2020001-2), Wenzhou Medical University (KYYW201901 and KYYW201906), Wenzhou Science and Technology Plan Project (Y20180071) and Start-up Scientific Research Foundation of Wenzhou Medical University (KYQD20190513).

Appendix A. Supplementary data

Supplementary data to this article can be found online at https://doi.org/10.1016/j.bioactmat.2021.01.035.

References

[1] S. Li, N. Chen, X. Li, Y. Li, Z. Xie, Z. Ma, J. Zhao, X. Hou, X. Yuan, Adv. Funct. Mater. 30 (2020) 2000130.
[2] D. Gan, T. Xu, W. Xing, X. Ge, L. Fang, K. Wang, F. Ren, X. Lu, Adv. Funct. Mater. 29 (2019) 1805964.
[3] B. Saleh, H.K. Dhaliwal, R. Portillo-Lara, E. Shirzaei Sani, R. Abdi, M.M. Amiji, N. Annabi, Small 15 (2019) 1902232.
[4] Y. Liang, X. Zhao, T. Hu, B. Chen, Z. Yin, P.X. Ma, B. Guo, Small 15 (2019) 1900046.
[5] S. Li, A. Chen, Y. Chen, Y. Yang, Q. Zhang, S. Luo, M. Ye, Y. Zhou, Y. An, W. Huang, Chem. Eng. J. 402 (2020) 126202.
[6] L. Han, X. Lu, K. Liu, K. Wang, L. Fang, L.T. Weng, H.P. Zhang, Y.H. Tang, F.Z. Ren, C.C. Zhao, ACS Nano 11 (2017) 2561–2574.
[7] Y. Wang, P. Zhou, D. Xiao, Y. Zhu, Y. Zhong, J. Zhang, X. Sui, X. Feng, H. Xu, Z. Mao, Carbohydr. Polym. 221 (2019) 202–208.
[8] Y. Yu, H. Yuk, G.A. Parada, Y. Wu, X. Liu, C.S. Nabzdyk, K. Youcef-Toumi, J. Zang, X. Zhao, Adv. Mater. 31 (2019) 1807101.
[9] S. Huang, H. Liu, K. Liao, Q. Hu, R. Guo, K. Deng, ACS Appl. Mater. Interfaces 12 (2020) 28952–28964.
[10] X. Yan, W.W. Fang, J. Xue, T.C. Sun, L. Dong, Z. Zha, H. Qian, Y.H. Song, M. Zhang, X. Gong, ACS Nano 13 (2019) 10074–10084.
[11] M. Konishi, Y. Tabata, M. Kariya, H. Hosseinkhani, A. Suzuki, K. Fukuhara, M. Mandai, K. Takakura, S. Fujii, J. Contr. Release 103 (2005) 7–19.
[12] E.S. Dragan, D. umelnicu, M.V. Dinu, I. Olariu, Chem. Eng. J. 330 (2017) 675–691.
[13] K. Ganguly, K. Chaturvedi, U.A. More, M.N. Nadagouda, T.M. Aminabhavi, J. Contr. Release 193 (2014) 162–173.
[14] B.W. Walker, R. Portillo Lara, E. Mogadam, C. Hsiang Yu, W. Kimball, N. Annabi, Prog. Polym. Sci. 92 (2019) 135–157.
[15] G. Sharifzadeh, H. Hosseinkhani, Adv. Healthc. Mater. 6 (2017) 1700801.
[16] C.F. Mao, W. Klinthong, Y.C. Zeng, C.H. Chen, Carbohydr. Polym. 89 (2012) 98–103.
[17] W. Khan, H. Hosseinkhani, D. Ickowicz, P.D. Hong, D.S. Yu, A.J. Domb, Acta Biomater. 8 (2012) 4224–4232.
[18] S.E. Harding, I.H. Smith, C.J. Lawson, R.J. Gahler, S. Wood, Carbohydr. Polym. 83 (2011) 329–338.
[19] K. Chen, F. Wang, S. Liu, X. Wu, L. Xu, D. Zhang, Int. J. Biol. Macromol. 148 (2020) 501–509.
[20] P. Tang, L. Han, P. Li, Z. Jia, K. Wang, H. Zhang, H. Tan, T. Guo, X. Lu, ACS Appl. Mater. Interfaces 11 (2019) 7703–7714.
[21] T. Zhou, L. Yan, C. Xie, P. Li, L. Jiang, J. Fang, C. Zhao, F. Ren, K. Wang, Y. Wang, Small 15 (2019) 1805440.
[22] Y. Li, C. Jiang, D. Zhang, Y. Wang, X. Ren, K. Ai, X. Chen, L. Lu, Acta Biomater. 47 (2017) 124–134.
[23] X. Qi, Q. Zeng, X. Tong, T. Su, L. Xie, K. Yuan, J. Xu, J. Shen, J. Hazard Mater. 402 (2021) 123359.
[24] X. Xu, X. Liu, L. Tan, Z. Cui, X. Yang, S. Zhu, Z. Li, X. Yuan, Y. Zheng, K.W. K. Yeung, Acta Biomater. 77 (2018) 352–364.
[25] D. Gan, W. Xing, L. Jiang, J. Fang, C. Zhao, F. Ren, L. Fang, K. Wang, X. Lu, Nat. Commun. 10 (2019) 1–10.
[26] L. Han, Y. Zhang, X. Lu, K. Wang, Z. Wang, H. Zhang, ACS Appl. Mater. Interfaces 8 (2016) 29088–29100.
[27] Y.Q. Zhao, Y. Sun, Y. Zhang, X. Ding, N. Zhao, B. Yu, H. Zhao, S. Duan, F.J. Xu, ACS Nano 14 (2020) 2265–2275.
[28] X. Bao, J. Zhao, J. Sun, M. Hu, X. Yang, ACS Nano 12 (2018) 8882–8892.
[29] X. Yang, T. Gong, D. Li, A. Li, L. Sun, Y. Guo, Carbohydr. Polym. 226 (2019) 115278.
[30] H. Shima, M. Sato, A. Inoue, Phys. Rev. E 93 (2016), 022406.
[31] Y. Zhu, Q. Zeng, Q. Zhang, K. Li, X. Shi, F. Liang, D. Han, Nanoscale 12 (2020) 8679–8686.
[32] J. Zhu, H. Han, F. Li, X. Wang, J. Yu, X. Qin, D. Wu, Chem. Mater. 31 (2019) 4436–4450.
[33] X. Qi, T. Su, M. Zhang, X. Tong, W. Pan, Q. Zeng, Z. Zhou, L. Shen, X. He, J. Shen, ACS Appl. Mater. Interfaces 12 (2020) 13256–13264.
[34] C.W. Hsiao, H.L. Chen, Z.X. Liao, R. Sureshbabu, H.C. Hsiao, S.J. Lin, Y. Chang, H. W. Sung, Adv. Funct. Mater. 25 (2015) 721–728.
[35] X. Zhao, Y. Liang, Y. Huang, J. He, Y. Han, B. Guo, Adv. Funct. Mater. 30 (2020) 1910748.
[36] C. Chen, J. Song, J. Cheng, Z. Pang, W. Gan, G. Chen, Y. Kuang, H. Huang, U. Ray, T. Li, ACS Nano (2020), https://doi.org/10.1021/acsnano.0c04298.
[37] E.S. Sani, R.P. Lara, Z. Aldawood, S.H. Bassir, D. Nguyen, A. Kantarci, G. Intini, N. Annabi, Matter 1 (2019) 926–944.
[38] C. Liu, W. Yao, M. Tian, J. Wei, Q. Song, W. Qiao, Biomaterials 179 (2018) 83–95.
[39] Y. Liang, B. Chen, M. Li, J. He, Z. Yin, B. Guo, Biomacromolecules 21 (2020) 1841–1852.
[40] J. He, M. Shi, Y. Liang, B. Guo, Chem. Eng. J. 394 (2020) 124888.